Complete electrode model in EEG: Relationship and differences to the point electrode model

S. Pursiainen†, F. Lucka§,‡ and C. H. Wolters§

†Aalto University, Mathematics, P.O. Box 11100, FI-00076 Aalto, Finland
§Institute for Biomagnetism and Biosignalanalysis, Westfälische Wilhelms-Universität Münster, Malmedyweg 15, 48149 Münster, Germany
‡Institute for Computational and Applied Mathematics, Westfälische Wilhelms-Universität Münster, Einsteinstrasse 62, 48149 Münster, Germany

E-mail: `Sampsa.Pursiainen@tkk.fi`

Abstract. In electroencephalography (EEG) source analysis, a primary current density generated by the neural activity of the brain is reconstructed from external electrode voltage measurements. This paper focuses on accurate and effective simulations of EEG through the complete electrode model (CEM). The CEM allows for the incorporation of the electrode size, shape and effective contact impedance (ECI) into the forward simulation. Both neural currents in the brain and shunting currents between the electrodes and the skin can affect the measured voltages in the CEM. The goal of this study was to investigate the CEM by comparing it to the point electrode model (PEM), which is the current standard electrode model for EEG. We used a three-dimensional, realistic and high-resolution finite element head model as the reference computational domain in the comparison. The PEM could be formulated as a limit of the CEM, in which the effective impedance of each electrode goes to infinity and the size tends to zero. Numerical results concerning the forward and inverse errors and electrode voltage strengths with different impedances and electrode sizes are presented. Based on the results obtained, limits for extremely high and low impedance values of the shunting currents are suggested.

PACS numbers: 87.19.le, 87.10.Kn, 02.30.Zz

AMS classification scheme numbers: 35Q60, 65M60, 15A29

1. Introduction

Nowadays electroencephalography (EEG) and magnetoencephalography (MEG) are widely used in various applications because of their non-invasiveness and their high spatio-temporal resolution (see e.g. (Niedermeyer & da Silva 2004, Hämäläinen et al. 1993)). In EEG and MEG source analysis (Sarvas 1987, Hämäläinen et al. 1993), a primary current density that is generated by the neural activity of the brain can be reconstructed by utilizing non-invasive field measurements on the surface of the head. Recovery of the primary current density is an ill-posed inverse problem, therefore effective inversion (reconstruction) (Dale & Sereno 1993, Phillips et al. 2002, Calvetti et al. 2009, Wipf & Nagarajan 2009) and forward simulation (data) (Schimpf et al. 2002, Hallez et al. 2005, Kybic et al. 2005, Tanzer et al. 2005, Wolters et al. 2007, Vallaghé & Papadopoulo 2010) methods are needed to produce appropriate reconstructions. Source analysis has already emerged as a promising tool for clinical applications. For example, it has been used in presurgical epilepsy diagnosis (Boon et al. 2002, Stefan et al. 2003) and in cognitive research (Hämäläinen et al. 1993, Haueisen & Knösche 2001). Due to the complementary sensitivities of EEG and MEG (Dassios et al. 2007), it was recently shown that simultaneous measurements (Heers et al. 2010) and a combined source analysis (Fuchs et al. 1998, Baillet et al. 1999, Huang et al. 2007, Sharon et al. 2007) of EEG and MEG are advantageous. However, the forward problem has to be modeled accurately in the combined analysis, in order to take into account the different sensitivity profiles of both modalities (Huang et al. 2007, Wolters et al. 2010).

The focus of this paper is on the accurate forward simulation of the electric potential, which is especially important for EEG and, to a lesser degree, also for MEG due to the dependence of MEG on the return currents (Wolters & de Munck 2007). Specifically, the boundary conditions of the complete electrode model (CEM) (Somersalo et al. 1992), that incorporates the electrode size, shape and effective contact impedance (ECI) into the forward simulation, were evaluated. The goal was to find out whether the CEM can lead to substantially different forward simulations for the electric potential or EEG inverse estimates as compared to the point electrode model (PEM), which is presently the most often utilized approach. In the PEM, the electrodes are associated with points (e.g., (Sarvas 1987, Hämäläinen et al. 1993, Schimpf et al. 2002, Hallez et al. 2005, Kybic et al. 2005, Wolters et al. 2007, Vallaghé & Papadopoulo 2010)) and neither the electrode size nor the impedance can be controlled. The CEM originates from electrical impedance tomography (EIT) (Cheney et al. 1999) and has been previously applied to EEG (Ollikainen et al. 2000, Pursiainen 2008*a*, Pursiainen 2008*b*, Calvetti et al. 2009). It has been shown (Ollikainen et al. 2000) that both the impedance and the surface area have an effect on the simulation of the electric potential in the case of a two dimensional domain. The present study investigates the described effect via finite element method (FEM) computations (Braess 2001) in 3D space.

In addition to using accurate boundary conditions, a realistic volume conductor model of a human head is needed to achieve the goal of accurate simulations for the electric potential. Therefore, in this present study, a considerable effort was made to model the head as realistically as possible. In line with the investigations of (Akhtari et al. 2002, Sadleir & Argibay 2007, Dannhauer et al. 2010), the skull in our realistic head model was modeled as consisting of three layers of outer and inner compacta that encloses the less resistive spongiosa. Taking into account that skull's apertures play an important role in source analysis (van den Broek et al. 1998, Oostenveld & Oostendorp 2002), the foramen magnum and the two optic canals were correctly modelled as skull openings. Furthermore, our head model included an accurate compartment for the highly conducting cerebrospinal fluid (CSF) (Baumann et al. 1997).

The importance of modeling the CSF as being situated between the sources in the brain and the measurement sensors was shown in sensitivity studies (Ramon et al. 2004, Wolters et al. 2006, Wendel et al. 2008). Finally, the inferior part of the model was not directly cut below the skull, as is often done in source analysis, but was realistically extended to avoid volume conduction modeling errors as reported previously (Bruno et al. 2003, Bruno et al. 2004, Lanfer et al. 2010).

The PEM and the corresponding forward simulation can be interpreted as a limit of the CEM, in which the impedance (ECI) of each electrode goes to infinity and the size tends to zero, as shown in this paper. Further, differences between the PEM and the CEM in the realistic head model were investigated using the PEM as the reference. This comparison utilizes lead-field matrices, which map the discretized primary current density $\mathbf{x}$ to the simulated electrode voltages $\mathbf{y}$ according to $\mathbf{y} = \mathbf{L}\mathbf{x}$. First, the forward simulation data that results from the CEM was studied for three alternative electrode diameters and various ECI values by examining column- and matrix-wise relative difference measures between CEM and PEM based lead-field matrices. Next, the performance of the CEM approach versus the PEM reference approach was investigated for inverse EEG source analysis scenarios.

In this paper, the theory section describes the CEM in combination with the resulting forward simulation, and shows how the infinite impedances and the PEM can be derived from the CEM. The method section describes model generation and parameter choices. The results section reports the forward and inverse source analysis experiments by focusing on the differences between the reference PEM and the different CEM results for the realistic head model. Finally, the discussion section summarizes and discusses the results and suggests possible topics for future work.

2. Theory

The EEG forward model associates a given primary current density $\mathbf{J}^p$ in the head Ω with a measurement data vector $\mathbf{y}$ containing electric potential values (Sarvas 1987, Hämäläinen et al. 1993). The data are obtained using a set of electrodes lying on the boundary $\partial\Omega$, i.e., the skin. A forward model that determines the voltage vector $\mathbf{U} = (U_1, U_2, \ldots, U_L)$ associated with the set of electrodes $e_1, e_2, \ldots, e_L$ given $\mathbf{J}^p$ plays a central role in the process of reconstructing $\mathbf{J}^p$ from noisy measurements of $\mathbf{U}$. The electric field $\mathbf{E}$ and the electric potential field u in Ω satisfy $\mathbf{E} = -\nabla u$, and the total current density is given by $\mathbf{J} = \mathbf{J}^p + \mathbf{J}^s = \mathbf{J}^p - \sigma\nabla u$, in which σ is the conductivity distribution in Ω and $\mathbf{J}^s = -\sigma\nabla u$ is the secondary current density. Substituting the total current density into the charge conservation law $\nabla\cdot\mathbf{J} = 0$ results into $\nabla\cdot(\sigma\nabla u) = \nabla\cdot\mathbf{J}^p$ in Ω. With appropriate primary current densities and boundary conditions, this equation is uniquely solvable (Evans 1998, Wolters et al. 2007) and can be used to model the potential distribution evoked by $\mathbf{J}^p$.

2.1. Forward simulation through CEM

This work concentrates on the boundary conditions of the CEM originally developed for EIT (Cheng et al. 1989, Somersalo et al. 1992). In the CEM, the contact electrodes are modeled as surface patches lying on the boundary $\partial\Omega$. Each electrode e_ℓ is associated with a real valued ECI denoted by Z_ℓ [$\Omega\mathrm{m}^2$]. The equation $\nabla\cdot(\sigma\nabla u) = \nabla\cdot\mathbf{J}^p$ is equipped with the boundary conditions

$$\sigma\nabla u\cdot\mathbf{n}|_{\partial\Omega\setminus\cup_\ell e_\ell} = 0, \quad \int_{e_\ell}\sigma\nabla u\cdot\mathbf{n}\,dS = 0 \quad\text{and}\quad (u+Z_\ell\sigma\nabla u\cdot\mathbf{n})|_{e_\ell} = U_\ell, \tag{1}$$

where $\ell = 1, 2, \ldots, L$. The first one ensures that the current flowing out or into the domain is zero over that part of the boundary which is not within the union $e_1\cup e_2\cup\cdots\cup e_L$. The second one states that the net current flowing through each electrode is zero. The third one describes how the electrode voltage U_ℓ depends on the potential field u, the normal derivative $\sigma\nabla u\cdot\mathbf{n}$ and Z_ℓ. Together these boundary conditions imply that the ℓ-th electrode voltage U_ℓ is the integral mean of u over e_ℓ given by $U_\ell = (\int_{e_\ell} u\,dS)/(\int_{e_\ell} dS)$, which can be verified through a straightforward calculation. Furthermore, defining the average contact impedance (ACI) of e_ℓ as $(\int_{e_\ell}|U_\ell - u|\,dS)/(\int_{e_\ell} dS\int_{e_\ell}\sigma|\nabla u\cdot\mathbf{n}|\,dS)$, i.e., as the average voltage difference divided by the integrated absolute value of the normal current density, the ECI equals to the ACI multiplied by the electrode surface area.

The boundary value problem of the CEM has the weak form (Somersalo et al. 1992, Vauhkonen 1997)

$$\int_\Omega \sigma\nabla u\cdot\nabla v\,dV + \sum_{\ell=1}^{L}\frac{1}{Z_\ell}\int_{e_\ell} u\,v\,dS - \sum_{\ell=1}^{L}\frac{1}{Z_\ell}\frac{\int_{e_\ell}u\,dS\int_{e_\ell}v\,dS}{\int_{e_\ell}dS} = -\int_\Omega(\nabla\cdot\mathbf{J}^p)v\,dV, \tag{2}$$

(Appendix) which, if we assume a sufficiently smooth primary current density $\mathbf{J}^p$, is uniquely solvable with $u \in H^1(\Omega) = \{w \in L^2(\Omega) : \partial w/\partial x_i \in L^2(\Omega),\ i = 1, 2, 3\}$ satisfying (2) for all $v \in H^1(\Omega)$. The weak form constitutes the present EEG forward model, i.e., the dependence of u on $\mathbf{J}^p$, which is linear with respect to $\mathbf{J}^p$ and well-defined for any $\mathbf{J}^p$ with a square integrable divergence. This study concentrates on the finite element discretizations of u and $\mathbf{J}^p$ given by $u_{\mathcal{T}} = \sum_{i=1}^N z_i\psi_i$ and $\mathbf{J}^p_{\mathcal{T}} = \sum_{i=1}^M x_i\,\mathbf{w}_i$ associated with the coordinate vectors $\mathbf{z} = (z_1, z_2, \ldots, z_N)$ and $\mathbf{x} = (x_1, x_2, \ldots, x_M)$, respectively. The functions $\psi_1, \psi_2, \ldots, \psi_N$ and $\mathbf{w}_1, \mathbf{w}_2, \ldots, \mathbf{w}_M$ are scalar and vector valued finite element basis functions defined on the finite element mesh $\mathcal{T}$ (Braess 2001) and the vectors $\mathbf{z}$ and $\mathbf{x}$ are linked through the linear system

$$\begin{pmatrix}\mathbf{A} & -\mathbf{B}\\ -\mathbf{B}^T & \mathbf{C}\end{pmatrix}\begin{pmatrix}\mathbf{z}\\ \mathbf{u}\end{pmatrix} = \begin{pmatrix}-\mathbf{G}\mathbf{x}\\ \mathbf{0}\end{pmatrix}, \tag{3}$$

which results from the Ritz-Galerkin type finite element discretization (Braess 2001) of the weak form (2), and is to be solved with respect to the electrode voltage vector $\mathbf{u} = (\mathbf{U}_1, \mathbf{U}_2, \ldots, \mathbf{U}_L)$. If $\psi_{i'}$ is a single arbitrary basis function lying on the part of the boundary $\partial\Omega \setminus \cup_\ell e_\ell$ not covered by the electrodes, the matrix $\mathbf{A} \in \mathbb{R}^{N\times N}$ can be defined by

$$a_{i,j} = \int_\Omega \sigma \nabla \psi_i \cdot \nabla \psi_j \, dV + \sum_{\ell=1}^{L} \frac{1}{Z_\ell} \int_{e_\ell} \psi_i \psi_j \, dS, \tag{4}$$

if neither i nor j equals i', and by $a_{i',i'} = 1$ and $a_{i',j} = a_{j,i'} = 0$, which hold if $j \neq i'$. The entries of $\mathbf{B} \in \mathbb{R}^{N\times L}$, $\mathbf{C} \in \mathbb{R}^{L\times L}$ and $\mathbf{G} \in \mathbb{R}^{N\times M}$ are given by

$$b_{i,\ell} = \frac{1}{Z_j} \int_{e_\ell} \psi_i \, dS, \tag{5}$$

$$c_{\ell,\ell} = \frac{1}{Z_\ell} \int_{e_\ell} dS \quad \text{and} \quad c_{i,\ell} = 0, \quad \text{if} \quad i \neq \ell, \tag{6}$$

$$g_{i,k} = \int_\Omega (\nabla \cdot \mathbf{w}_k) \psi_i \, dV. \tag{7}$$

The measurement data vector, given by $\mathbf{y} = \mathbf{Ru}$, contains the electrode voltages with respect to the potential zero reference level, that is here the sum of the electrode voltages. The entries of $\mathbf{R} \in \mathbb{R}^{L\times L}$ are given by $r_{j,j} = 1 - 1/L$ for $j = 1, 2, \ldots, L$, and $r_{i,j} = -1/L$ for $i \neq j$. Solving $\mathbf{u}$ from (3) results into the equation $\mathbf{y} = \mathbf{R}(\mathbf{B}^T\mathbf{A}^{-1}\mathbf{B} - \mathbf{C})^{-1}\mathbf{B}^T\mathbf{A}^{-1}\mathbf{Gx}$, which yields the lead field matrix

$$\mathbf{L}_{\mathbf{CEM}} = \mathbf{R}(\mathbf{B}^T\mathbf{A}^{-1}\mathbf{B} - \mathbf{C})^{-1}\mathbf{B}^T\mathbf{A}^{-1}\mathbf{G}. \tag{8}$$

In equation (8), because $N \gg L$ (in this paper, we have $N = 628\,032$ and $L = 79$), efficient computation of $T := B^T A^{-1} \in \mathbb{R}^{L\times N}$ is obtained through $B^T = TA \Leftrightarrow B = A^T T^T = AT^T$, where the symmetry of A is used in the last step. The transfer matrix T can then be computed efficiently using iterative solver methods (Wolters et al. 2004, Lew et al. 2009).

2.2. Shunting effects

As the electrodes are used to passively measure the potential distribution evoked by the primary source current, it is assumed that the net current flowing through each electrode e_ℓ is zero, i.e., $\int_{e_\ell} \sigma \nabla u \cdot \mathbf{n} \, dS = 0$. In addition to the net current, the CEM allows the existence of a nonzero shunting (Ollikainen et al. 2000) current density $(\sigma \nabla u \cdot \mathbf{n})|_{e_\ell}$ between the electrode e_ℓ and the skin. Shunting effects cause a power loss of the simulated signal and alter the voltage pattern in the measurements. The magnitude of $(\sigma \nabla u \cdot \mathbf{n})|_{e_\ell}$ is affected by Z_ℓ: the lower the ECI the higher the current. Further, if each ECI goes to infinity, then the boundedness of the weak form (2) enforces $(\sigma \nabla u \cdot \mathbf{n})|_{e_\ell}$ to tend to zero for $\ell = 1, 2, ..., L$, i.e., the power loss due to the electrodes vanishes resulting into the strongest possible simulated signal. Note that extremely high ECIs (e.g. 10^6 Ωm^2) are, however, disadvantageous for the practical signal strength, since the EEG amplifier has a finite input-impedance and signal-to-noise ratio (Niedermeyer & da Silva 2004).

2.3. Infinite impedances

If $Z_1 = Z_2 = \cdots = Z_L = \infty$ the CEM boundary conditions (1) reduce to the standard Neumann condition $(\sigma \nabla u \cdot \mathbf{n})|_{\partial\Omega} = 0$, i.e., the current flowing out or into the domain is zero everywhere. Similar to the case of finite impedances, the ℓ-th electrode voltage is the integral mean of u over e_ℓ. Defining the matrices $\mathbf{A}' \in \mathbb{R}^{N\times N}$, $\mathbf{B}' \in \mathbb{R}^{N\times L}$ and $\mathbf{C}' \in \mathbb{R}^{L\times L}$ by replacing the expressions for $a_{i,j}$, $b_{i,\ell}$ and $c_{i,\ell}$ in (4), (5) and (6) with $a'_{i,j} = \int_\Omega \sigma \nabla\psi_i \cdot \nabla\psi_j \, dV$, $b'_{i,\ell} = \int_{e_\ell} \psi_i \, dS$ and $c'_{\ell,\ell} = \int_{e_\ell} dS$, the lead field matrix can be written as

$$\mathbf{L}_{\mathbf{CEM}\infty} = -\mathbf{R}\mathbf{C}'^{-1}\mathbf{B}'^{T}\mathbf{A}'^{-1}\mathbf{G}. \tag{9}$$

This matrix can be derived from the weak form (2) omitting the terms involving the impedances or from (8) by choosing $Z_1 = Z_2 = \cdots = Z_L = t \to \infty$ and calculating the limit $\lim_{t\to\infty} \mathbf{L}_{\mathbf{CEM}} = \lim_{t\to\infty} \mathbf{R}(t^{-2}\mathbf{B}'^{T}\mathbf{A}^{-1}\mathbf{B}'^{T} - t^{-1}\mathbf{C}')^{-1} t^{-1}\mathbf{B}'^{T}\mathbf{A}^{-1}\mathbf{G} = \lim_{t\to\infty} \mathbf{R}(t^{-1}\mathbf{B}'^{T}\mathbf{A}^{-1}\mathbf{B}'^{T} - \mathbf{C}')^{-1}\mathbf{B}'^{T}\mathbf{A}^{-1}\mathbf{G} = \mathbf{L}_{\mathbf{CEM}\infty}$.

2.4. Forward simulation through PEM

In the classical point electrode model (PEM), the electrodes $e_1, e_2, \ldots, e_L$ are assumed to coincide with the points p_1, p_2, $\ldots$, p_L, respectively, and the Neumann boundary condition $(\partial\sigma\nabla u/\partial\mathbf{n})|_{\partial\Omega} = 0$ is used instead of (1). Defining $\mathbf{B}''$ by replacing (5) with $b''_{i,\ell} = \psi_i(p_\ell)$ the PEM lead field matrix is given by

$$\mathbf{L}_{\mathbf{PEM}} = -\mathbf{R}\mathbf{B}''^{T}\mathbf{A}'^{-1}\mathbf{G}, \tag{10}$$

which is also the limit of $\mathbf{L}_{\mathbf{CEM}\infty}$ as $e_1, e_2, \ldots, e_L$ shrink to $p_1, p_2, \ldots, p_L$. Namely, according to the integral mean value theorem, $b'_{i,\ell}/c'_{\ell,\ell} = (\int_{e_\ell} \psi_i \, dS)/(\int_{e_\ell} dS) \to \psi_i(p_\ell) = b''_{i,\ell}$ if e_ℓ shrinks continuously to p_ℓ and ψ_i is continuous.

3. Methods

3.1. Head model generation

T1- and T2- weighted magnetic resonance images (MRI) of a healthy 24 year old male subject were measured on a 3T MR scanner. A T1w pulse sequence with fat suppression and a T2w pulse sequence with minimal water-fat-shift, both with an isotropic resolution of $1,17 \times 1,17 \times 1,17$ mm, were used. The T2-MRI was registered onto the T1-MRI using an affine registration approach and mutual information as a cost-function as implemented in *FSL* ‡. The compartments skin, skull compacta and skull spongiosa were segmented using a grey-value based active contour model (Vese & Chan 2002) and thresholding techniques. The segmentation was carefully checked and corrected manually. Because of the importance of skull holes on source analysis (van den Broek et al. 1998, Oostenveld & Oostendorp 2002), the foramen magnum and the two optic canals were correctly modelled as skull openings. Following (Bruno et al. 2003, Bruno

---

‡ FLIRT - FMRIB's Linear Image Registration Tool, http://www.fmrib.ox.ac.uk/fsl/flirt/index.html

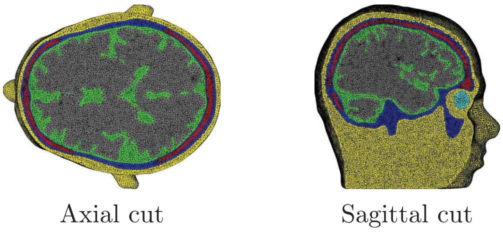

Figure 1. Visualization of the used tetrahedral finite element head model opened by an axial (left) and a sagittal (right) cut. The model consists of the following compartments: grey matter (grey), CSF (green), compact bone (blue), spongy bone (red), skin (yellow), and the eyes (light blue). Visualization was carried out using the *SCIRun* software (The SCIRun Team n.d.).

et al. 2004, Lanfer et al. 2010), the inferior part of the model was not directly cut below the skull, but was realistically extended to avoid volume conduction modeling errors. The software *CURRY* § was then used for the segmentation of the cortex surface as well as the extraction of high resolution meshes of the surfaces of skin, eyes, skull compacta, skull spongiosa and brain from the voxel-based segmentation volumes. The surfaces were smoothed using Taubin smoothing (Taubin 1995) to remove the blocky structure which results from the fine surface sampling of the voxels. The smoothed surfaces were then used to create a high quality 3D Delaunay triangulation via *TetGen*‖. In total, the resulting tetrahedral finite element (FE) model consists of $N = 628\,032$ nodes and 3 912 563 tetrahedral elements. The conductivity values (in S/m) for the different compartments were chosen to be 0.43 for skin (Dannhauer et al. 2010), 0.0064 for skull compacta and 0.02865 for skull spongiosa (Akhtari et al. 2002, Dannhauer et al. 2010), 1.79 for the CSF (Baumann et al. 1997), 0.33 for the brain (Dannhauer et al. 2010) and 0.505 for the eyes (Ramon et al. 2006). The resulting tetrahedral FE model is shown in figure 1.

3.2. Electrode configurations

A number of 79 surface electrodes ($L = 79$) were positioned on the head surface according to the 10/10 system using the software CURRY. The CEM-based lead field matrix $\mathbf{L}$ was computed for three sets of circular electrodes with diameters $d = 6, 12$, and 18 mm (figure 2). All the electrodes were assumed to have an identical ECI, denoted here by Z, and given the values $10^{-6}, 10^{-5}, \ldots, 1, \ldots, 10^{5}, 10^{6}$ and ∞ in Ωm^2 . The results obtained were plotted against the ECI, one curve for each applied electrode size.

---

§ CURrent Reconstruction and Imaging (CURRY), http://www.neuroscan.com/

‖ TetGen: A Quality Tetrahedral Mesh Generator and a 3D Delaunay Triangulator, http://tetgen.berlios.de/

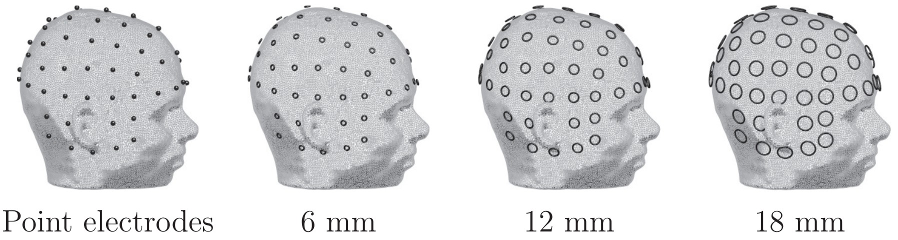
Point electrodes 6 mm 12 mm 18 mm

Figure 2. Point electrodes and patch electrodes with diameters 6, 12 and 18 mm, respectively, visualized on the triangular outer surface of the finite element mesh.

3.3. *Finite element basis functions*

The potential distribution was discretized using linear Lagrangian basis functions $\psi_1, \psi_2, \ldots, \psi_N$ (Braess 2001, Solin et al. 2003) on the tetrahedral mesh. The basis function ψ_i obtains the value one in the i-th mesh node and vanishes in all the other nodes. Consequently, the value of $u_{\mathcal{T}}$ at the i-th node coincides with the i-th degree of freedom z_i of $u_{\mathcal{T}}$. Restriction of the linear basis function to a single tetrahedron can be obtained requiring that its value equals one in a single vertex. The resulting basis functions are piecewise continuous and form a subspace of $H^1(\Omega)$.

Lowest order Raviart-Thomas (Braess 2001, Monk 2003, Pursiainen et al. 2011) basis functions $\mathbf{w}_1, \mathbf{w}_2, \ldots, \mathbf{w}_M$ (figure 3) were used to discretize the primary current density. Each $\mathbf{w}_k$ is supported on two adjacent tetrahedral elements sharing the k-th face of the finite element mesh. Restriction of $\mathbf{w}_k$ to one of the supporting tetrahedrons is proportional to the position vector field with the origin at the vertex opposite to the k-th face. The normal component of $\mathbf{w}_k$ is continuous over the k-th face and zero on all the other faces. The scaling of $\mathbf{w}_k$ is such that the resulting dipole moment $\mathbf{q}_k = \int_\Omega \mathbf{w}_k dV$ (Pursiainen et al. 2011) is of unit length, i.e. $\|\mathbf{q}_k\|_2 = 1$. As a result, the divergence of $\mathbf{w}_k$ is square integrable.

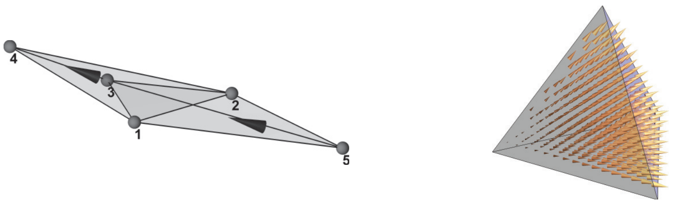

Figure 3. On the left: A lowest order Raviart-Thomas basis function is supported on two adjacent tetrahedral elements. On the right: The vector field of a Raviart-Thomas basis function restricted to one tetrahedral element.

3.4. *PEM and CEM difference measures with regard to CEM electrode diameter and ECI*

3.4.1. Global lead-field difference measures The dependence of the forward simulation results on the electrode diameter and the ECI will be studied in an experiment, in which the lead-field matrices are compared in terms of the global difference measures (global with regard to the whole brain influence space) RE (relative error), RDM (relative-difference measure) and RN (relative norm) given by

$$\mathrm{RE} = \sqrt{\sum_{k=1}^{M} \|\mathbf{l}_k - \mathbf{l}_k^{\mathrm{REF}}\|_2^2 \Big/ \sum_{k=1}^{M} \|\mathbf{l}_k^{\mathrm{REF}}\|_2^2}, \tag{11}$$

$$\mathrm{RDM} = \sqrt{\frac{1}{M} \sum_{k=1}^{M} \left\| \mathbf{l}_k / \|\mathbf{l}_k\|_2 - \mathbf{l}_k^{\mathrm{REF}} / \|\mathbf{l}_k^{\mathrm{REF}}\|_2 \right\|_2^2}, \tag{12}$$

$$\mathrm{RN} = \sqrt{\sum_{k=1}^{M} \|\mathbf{l}_k\|_2^2 \Big/ \sum_{k=1}^{M} \|\mathbf{l}_k^{\mathrm{REF}}\|_2^2}. \tag{13}$$

Because the PEM is currently the standard electrode model in source analysis, we defined it as our reference. The vector $\mathbf{l}_k^{\mathrm{REF}}$ is the k-th column of the reference matrix $\mathbf{L}^{\mathrm{REF}}$ computed through the PEM with the same conductivity distribution and set of dipole moment and location pairs as in the computation of $\mathbf{L}$, for which the CEM will be used. Similar to the measures introduced by (Meijs et al. 1989), the RE is sensitive to both topography as well as magnitude differences between PEM and CEM lead-fields, the RDM is a measure of lead-field topography differences and the RN is sensitive to differences in PEM and CEM lead-field magnitudes. A PEM and a CEM lead-field are maximally similar, i.e., identical, if RE and RDM are at 0 and RN is at 1. The maximum for the RDM is a value of 2 (Lew et al. 2009).

3.4.2. Local lead-field difference measures In the second experiment, the distribution of the local or column-wise forward and inverse errors in the brain compartment will be studied. As the forward error, the column-wise relative difference measure

$$\mathrm{RDM}_k = \left\| \mathbf{l}_k / \|\mathbf{l}_k\|_2 - \mathbf{l}_k^{\mathrm{REF}} / \|\mathbf{l}_k^{\mathrm{REF}}\|_2 \right\|_2 \tag{14}$$

will be used as a measure of topography differences between PEM and CEM forward simulation results for the k-th source. A PEM and a CEM forward simulation for source k is maximally similar, i.e., identical, if RDM_k is at 0, and the difference is maximal if RDM_k is at 2 (Lew et al. 2009).

3.4.3. Inverse localization difference measures The inverse single source analysis aspect will be examined utilizing the PE (placement error) and the AE (angular error) for the Raviart-Thomas type source $(\mathbf{q}_k, \mathbf{r}_k)$ (Pursiainen et al. 2011) with position $\mathbf{r}_k$ and moment $\mathbf{q}_k$, i.e.,

$$\mathrm{PE}_k = \|\mathbf{r}_{j_k} - \mathbf{r}_k\|_2 \quad \text{and} \quad \mathrm{AE}_k = |\arccos(\mathbf{q}_{j_k} \cdot \mathbf{q}_k)|, \tag{15}$$

in which $j_k = \arg\min_j \|\mathbf{l}_j - \mathbf{l}_k^{\mathrm{REF}}\|_2$ corresponds to the Raviart-Thomas type source $(\mathbf{q}_{j_k}, \mathbf{r}_{j_k})$ that best reproduces the reference data $\mathbf{l}_k^{\mathrm{REF}}$ in terms of the maximum likelihood.

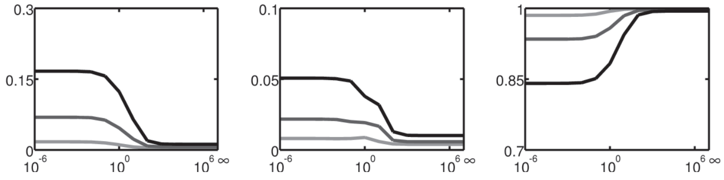

RE RDM RN

Figure 4. The difference measures RE, RDM and RN between PEM and CEM visualized as a function of the CEM effective contact impedance Z, common for all the electrodes. The electrode diameters 6 mm, 12 mm and 18 mm correspond to light grey, dark grey and black curves, respectively.

4. Results

Each forward simulation strategy was used to produce a set of lead-field matrices of the form $\mathbf{L} = (\mathbf{l}_1, \mathbf{l}_2, \ldots, \mathbf{l}_M)$, with $\mathbf{l}_k$ corresponding to data evoked by a single Raviart-Thomas type dipole-like source (Pursiainen et al. 2011) with the direction $\mathbf{q}_k = \int_\Omega \mathbf{w}_k \, \mathrm{d}V$, $\|\mathbf{q}_k\|_2 = 1$ (unit dipole moment) and the location $\mathbf{r}_k$ that is the midpoint of the line segment between nodes 4 and 5 (figure 3). The number of rows and columns in the lead-field matrix coincided with the number of electrodes and that of source locations, respectively.

4.1. Global PEM and CEM forward modeling differences

Figure 4 shows the results and reveals that, with increasing ECI, differences between the reference PEM and the CEM lead-fields decrease, expressed by decreasing RE and RDM measures and an RN that approaches 1. The slope of the curves presented in figure 4 is relatively steep between 10^{-2} and 10^{2} $\Omega\mathrm{m}^2$, and it is rather flat between 10^{-6} and 10^{-2} $\Omega\mathrm{m}^2$ as well as from 10^{2} $\Omega\mathrm{m}^2$ to ∞. Differences between PEM and CEM lead-fields also decreased with a decreasing electrode diameter, expressed by decreasing RE and RDM and an RN that approaches 1. The biggest difference between PEM and CEM lead-fields was found for lowest ECI and highest electrode diameter, expressed by an RE of 0.167, an RDM of 0.051 and an RN of 0.841.

4.2. Local PEM and CEM forward modeling differences

In the second experiment, the distribution of the local or column-wise forward modeling differences in the brain compartment were studied.

Maximum and mean values of the RDM_k, $k = 1, 2, \ldots, M$, have been documented in table 1. Furthermore, the distribution of $\max_k \mathrm{RDM}_k$ is shown in figures 5 (visualized on cortex) and 6 (visualized on mid-sagittal cross-section) covering the electrode diameters $d = 6, 12,$ and 18 mm, as well as the ECIs $Z = 10^{-6}$, 1 and 10^{6} $\Omega\mathrm{m}^2$. In visualization of RDM_k, a decibel (dB) scale was utilized with the maximum $\max_k \mathrm{RDM}_k$ fixed to 0 dB in order to enable a common scaling throughout the comparison.

Table 1. Maximum and mean of RDM_k with different electrode sizes and values of the effective impedance.

		Electrode diameter		
Type	ECI[a] ($\Omega\mathrm{m}^2$)	6 mm	12 mm	18 mm
Maximum	10^{-6}	0.0262	0.0642	0.112
Maximum	1	0.0238	0.0498	0.0887
Maximum	10^{6}	0.0180	0.0361	0.0606
Mean	10^{-6}	0.00775	0.0207	0.0486
Mean	1	0.008360	0.0186	0.0362
Mean	10^{6}	0.00377	0.00523	0.00888

[a] Effective contact impedance

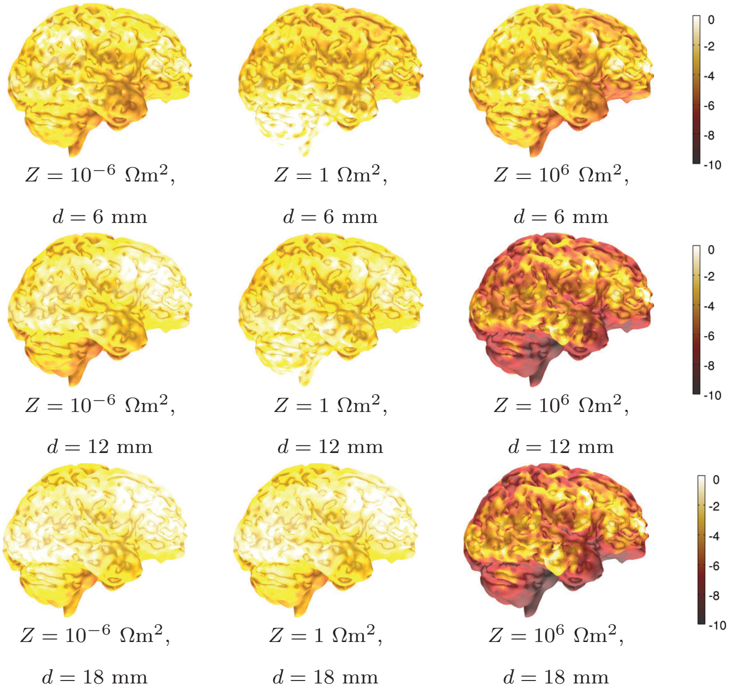

$Z = 10^{-6}\ \Omega\mathrm{m}^2$, $d = 6$ mm; $Z = 1\ \Omega\mathrm{m}^2$, $d = 6$ mm; $Z = 10^{6}\ \Omega\mathrm{m}^2$, $d = 6$ mm

$Z = 10^{-6}\ \Omega\mathrm{m}^2$, $d = 12$ mm; $Z = 1\ \Omega\mathrm{m}^2$, $d = 12$ mm; $Z = 10^{6}\ \Omega\mathrm{m}^2$, $d = 12$ mm

$Z = 10^{-6}\ \Omega\mathrm{m}^2$, $d = 18$ mm; $Z = 1\ \Omega\mathrm{m}^2$, $d = 18$ mm; $Z = 10^{6}\ \Omega\mathrm{m}^2$, $d = 18$ mm

Figure 5. The local relative difference measure RDM_k visualized on the cortical surface utilizing the decibel (dB) scale. The zero decibel level has been associated with the maximum entry $\max_k \mathrm{RDM}_k$. Different images correspond to different combinations of the effective contact impedance Z and of the electrode diameter denoted by d.

Maximum and mean values of RDM_k documented in table 1 were generally the higher the lower Z and the larger d was. The highest documented maximum and mean 0.112 and 0.0486, respectively, were obtained with $Z = 10^{-6}\ \Omega\mathrm{m}^2$ and $d = 18$ mm. The mean value of RDM_k was particularly low, less than 0.01, when either Z was $10^6\ \Omega\mathrm{m}^2$ or d was 6 mm. Figures 5 and 6 show that the highest values of RDM_k occurred almost

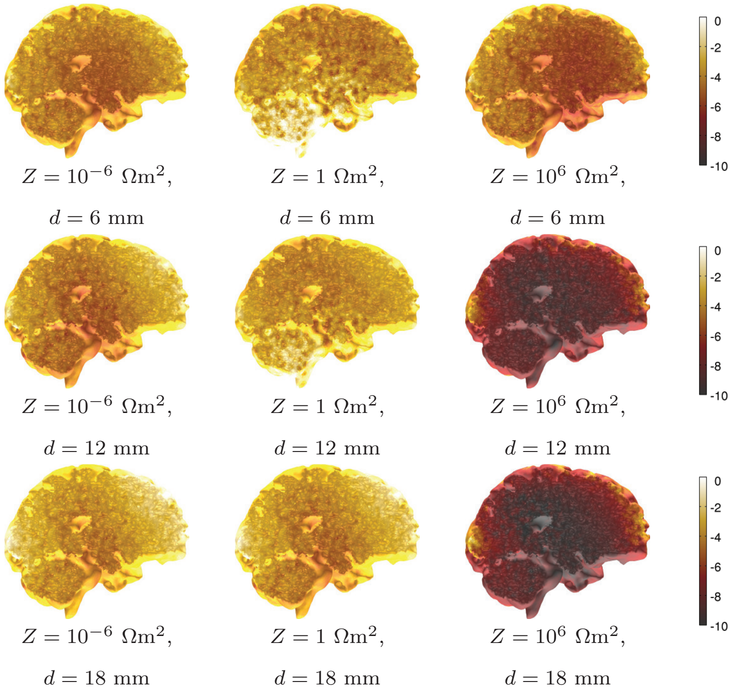

$Z = 10^{-6}\ \Omega\mathrm{m}^2$, $d = 6$ mm
$Z = 1\ \Omega\mathrm{m}^2$, $d = 6$ mm
$Z = 10^{6}\ \Omega\mathrm{m}^2$, $d = 6$ mm

$Z = 10^{-6}\ \Omega\mathrm{m}^2$, $d = 12$ mm
$Z = 1\ \Omega\mathrm{m}^2$, $d = 12$ mm
$Z = 10^{6}\ \Omega\mathrm{m}^2$, $d = 12$ mm

$Z = 10^{-6}\ \Omega\mathrm{m}^2$, $d = 18$ mm
$Z = 1\ \Omega\mathrm{m}^2$, $d = 18$ mm
$Z = 10^{6}\ \Omega\mathrm{m}^2$, $d = 18$ mm

Figure 6. The local relative difference measure RDM_k visualized on the mid-sagittal cross-section utilizing the decibel (dB) scale. The zero decibel level has been associated with the maximum entry $\max_k \mathrm{RDM}_k$. Different images correspond to different combinations of the effective contact impedance Z and of the electrode diameter denoted by d.

in all cases in lateral areas of the source space close to the electrodes. With $Z = 1\ \Omega\mathrm{m}^2$ and the electrode diameter $d = 6$ mm, RDM_k was exceptionally the highest in cerebellar areas. Based on figures 5 and 6, it is also obvious that the gradient of RDM_k was the stronger the larger were the values of Z and d; with a high Z (e.g., $10^6\ \Omega\mathrm{m}^2$) and a large enough d (e.g., 12 or 18 mm), RDM_k decayed rapidly when moving away from the lateral areas of the source space close to the electrodes towards the depth of the brain resulting into a high relative difference between the maximum and mean value of RDM_k (table 1).

4.3. PEM and CEM differences in inverse source localization

In the last experiment with regard to inverse source analysis, the distributions of PE_k and AE_k were visualized in figures 7 and 8 and their maximum and mean values were reported in tables 2 and 3. PE_k and AE_k were illustrated using the millimeter and the degree scale, respectively.

PE_k and AE_k were zero in large part of their distributions, and the peak values occurred rather randomly. In contrast to RDM_k, the weight of the distribution of the placement error PE_k seemed to be rather concentrated on inferior than on superior areas of the source space (figures 7 and 8), at least with the electrode diameter of 18 mm.

Table 2. Maximum and mean of PE_k (mm) with different electrode sizes and values of the effective impedance.

		Electrode diameter		
Type	ECI[a] ($\Omega\mathrm{m}^2$)	6 mm	12 mm	18 mm
Maximum	10^{-6}	1.90	15.3	25.8
Maximum	1	0	10.3	24.6
Maximum	10^{6}	0	0	0
Mean	10^{-6}	$1.62 \cdot 10^{-4}$	0.363	7.83
Mean	1	0	0.0288	4.39
Mean	10^{6}	0	0	0

[a] Effective contact impedance

Table 3. Maximum and mean of AE_k (degrees) with different electrode sizes and values of the effective impedance.

		Electrode diameter		
Type	ECI[a] ($\Omega\mathrm{m}^2$)	6 mm	12 mm	18 mm
Maximum	10^{-6}	1.83	31.1	54.8
Maximum	1	0	27.6	52.9
Maximum	10^{6}	0	0	0
Mean	10^{-6}	$1.57 \cdot 10^{-4}$	0.475	8.88
Mean	1	0	0.0449	5.08
Mean	10^{6}	0	0	0

[a] Effective contact impedance

The angular error AE_k again seemed to be very randomly distributed over the source space (figures 7 and 8). Like for RDM_k, the maximum and the mean of PE_k and AE_k (tables 2 and 3) increased as d was grown or Z decreased. With the ECI of $Z = 10^6$ $\Omega\mathrm{m}^2$, both of these errors vanished independently on the electrode size. For an electrode diameter of 6 mm, PE_k and AE_k also vanished for $Z = 1$ $\Omega\mathrm{m}^2$, and the errors obtained with $Z = 10^{-6}$ $\Omega\mathrm{m}^2$ were very small ($\max_k \mathrm{PE}_k \leq 1.90$ mm and $\max_k \mathrm{AE}_k \leq 1.83^\circ$). The maximum and the mean of PE_k and AE_k were as large as 25.8 mm, 7.83 mm, 54.8° and 8.88°, respectively, with $d = 18$ mm, and $Z = 10^{-6}$ $\Omega\mathrm{m}^2$.

5. Discussion

Currently, the point electrode model (PEM) is the standard for the forward simulation in electroencephalography (EEG) and also in magnetoencephalography (MEG) source analysis regarding following forms of volume conductor modeling: spherical (de Munck

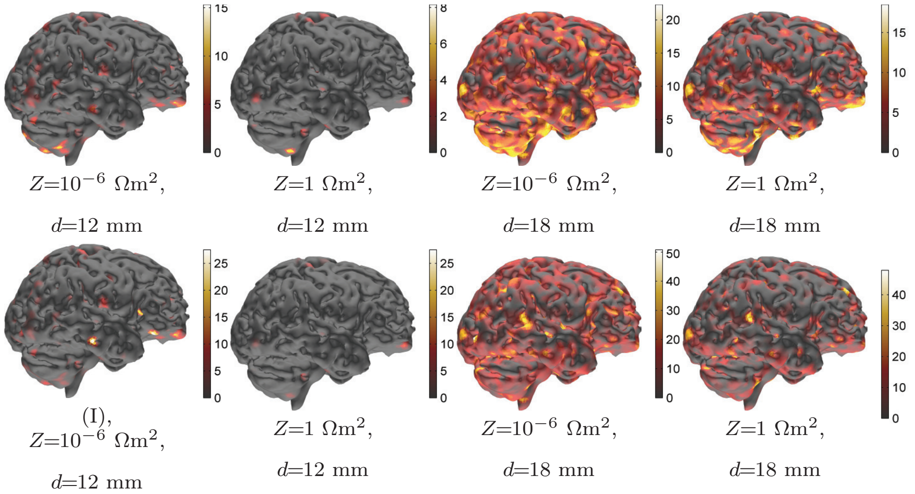

Z=10^{-6} Ωm^2, d=12 mm

Z=1 Ωm^2, d=12 mm

Z=10^{-6} Ωm^2, d=18 mm

Z=1 Ωm^2, d=18 mm

(I), Z=10^{-6} Ωm^2, d=12 mm

Z=1 Ωm^2, d=12 mm

Z=10^{-6} Ωm^2, d=18 mm

Z=1 Ωm^2, d=18 mm

Figure 7. The placement error PE$_k$ (upper row) and the angular error AE$_k$ (lower row) visualized on the cortical surface with different combinations of the effective contact impedance Z and the electrode diameter denoted by d.

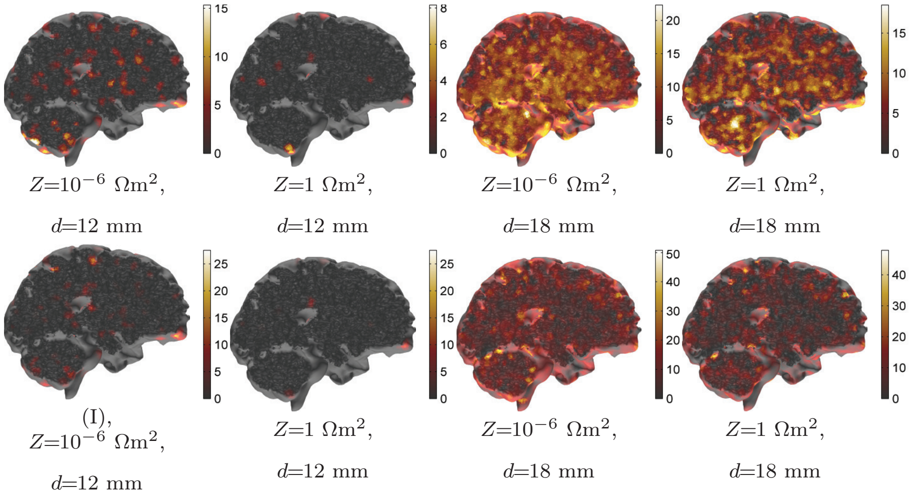

Z=10^{-6} Ωm^2, d=12 mm

Z=1 Ωm^2, d=12 mm

Z=10^{-6} Ωm^2, d=18 mm

Z=1 Ωm^2, d=18 mm

(I), Z=10^{-6} Ωm^2, d=12 mm

Z=1 Ωm^2, d=12 mm

Z=10^{-6} Ωm^2, d=18 mm

Z=1 Ωm^2, d=18 mm

Figure 8. The placement error PE$_k$ (upper row) and the angular error AE$_k$ (lower row) visualized on the mid-sagittal cross-section, with different combinations of the effective contact impedance Z and the electrode diameter denoted by d.

& Peters 1993), boundary element method (Sarvas 1987, Hämäläinen et al. 1993, Kybic et al. 2005), finite difference method (Hallez et al. 2005), finite volume method (Cook & Koles 2006) and finite element method (FEM) (Schimpf et al. 2002, Wolters et al. 2007, Vallaghé & Papadopoulo 2010). This paper dealt with the EEG and the complete electrode model (CEM) boundary conditions that allow the incorporation of electrode size, shape and effective contact impedance (ECI) into the forward simulation. The CEM boundary conditions were formulated for the EEG, with regard to the finite and infinite ECI. The classical PEM was derived from the CEM equations by setting the electrode diameter to zero and the ECI to infinity. The differences in the forward simulations that resulted from the CEM and the PEM were studied in numerical experiments from both the forward and inverse aspects. The FEM was used to implement the PEM and the CEM and a three-dimensional, realistic and highly resolved FEM head model was used as the reference computational domain. Each tested forward simulation strategy was used to produce a set of lead-field matrices, in which each column corresponded to data evoked by a single Raviart-Thomas type dipole-like source. The forward aspect was analyzed by using the following parameters: the relative error (RE), to measure topography and magnitude differences, the relative norm (RN) to measure magnitude differences, and the matrix- (RDM) and column-wise (RDM_k) relative difference measure to measure topography differences between PEM and CEM lead-fields. Because the PEM is the standard at present, it was used as the reference in our investigations. The inverse aspect was approached by examining the placement and the angular error PE_k and AE_k in a source localization procedure.

The numerical results for RN, RE and RDM were in good correspondence with the derivation (Section 2.4) that the PEM follows on from the CEM when the electrode diameter shrinks to zero and the ECI goes to infinity. On one hand, the RDM and RE curves had a decreasing tendency and the RN approached one, which showed that both topography and magnitude differences between PEM and CEM decreased with increasing ECI. On the other hand, when the smallest utilized electrode diameter (6 mm) was used, both RE and RDM were found to be substantially closer to zero, and RN was closer to one than with the two larger diameter electrodes. This finding suggests that the CEM based lead-field matrices are close to those obtained with the PEM, when the electrodes are small. The decreasing magnitude differences found between PEM and CEM with increasing ECI obviously had resulted from a growing signal strength indicated by RN. This is due to the phenomenon that the higher the impedance, the weaker the shunting effects. An interesting feature in RE, RN and RDM is the steep slope located approximately between $Z = 10^{-2}\ \Omega\mathrm{m}^2$ and $Z = 10^{2}\ \Omega\mathrm{m}^2$, which suggests that the ECI can be labeled as extremely low (maximal shunting), intermediate, or extremely high (minimal shunting) based on whether it is below $10^{-2}\ \Omega\mathrm{m}^2$, belongs to the interval between $10^{-2}\ \Omega\mathrm{m}^2$ and $10^{2}\ \Omega\mathrm{m}^2$ or is above $10^{2}\ \Omega\mathrm{m}^2$, respectively. If the shunting effect is minimal or maximal, the measurements will be sensitive to noise. The sensitivity to noise arises because the signal power captured by the electrodes is very low due to vanishing voltage differences on the electrodes at shunting maximum and due to the extremely low shunting currents at shunting minimum.

The results of the local or column-wise error measures RDM_k, PE_k and AE_k were computed using ECIs 10^{-6}, 1, and $10^{6}\ \Omega\mathrm{m}^2$ that cover the three intervals (Z values) suggested above. With the extremely high value ($Z = 10^{6}\ \Omega\mathrm{m}^2$), the CEM and PEM provided very similar forward simulations. The local relative difference measure RDM_k decayed very rapidly when moving away from the electrodes and no source localization errors were detected, as both the placement and the angular error PE_k and AE_k vanished everywhere. In the intermediate case ($Z = 1\ \Omega\mathrm{m}^2$), the distribution of RDM_k was much more even throughout the cortical surface, and the source localization errors differed from zero for the two largest electrode sizes. Again, with the extremely low value ($Z = 10^{-6}$ Ωm^2), the distribution of RDM_k was relatively high everywhere, and PE_k and AE_k were non-zero, independent of the electrode size.

As shown by figures 5 and 6, the forward errors are not simply below the electrodes due to a complicated interplay between impedance value, electrode surface and volume conduction, especially the effect of the strongly folded cortical surface in our realistic head model. Even if figure 6, especially the case with high impedance and large electrode surface, show the tendency that the CEM-PEM differences rapidly decrease with distance to the electrodes, the effects are not simply limited to the cortical areas directly beneath the electrodes. Further, it is natural that the largest placement errors were rather concentrated on inferior than on superior areas of the source space, since the source localization problem is particularly ill-conditioned for sources lying deep within the brain. The fact that the inverse errors do not clearly follow any other pattern is at least partially due to the applied source localization strategy.

Namely, although the forward simulation differences presented above are comprehensively due to the differences between PEM and CEM modeling, the situation is more complex for the inverse reconstruction results. It is inherent that the differences in the forward modeling and limitations of the chosen inverse procedure are intermixed. Consequently, the placement and angular errors obtained in our investigations are mainly due to two aspects: namely the differences between PEM and CEM and also the errors introduced by the inverse reconstruction procedure. The Raviart-Thomas source model was developed recently (Pursiainen et al. 2011) and the interplay between the inverse methods available in the EEG and MEG source analysis literature and this new source model has not yet been sufficiently investigated. The inverse reconstruction procedure used in this study and also in an earlier study (Pursiainen et al. 2011) is clearly different from the dipole fit approach (Scherg & von Cramon 1985, Mosher et al. 1992) and the goal function scan (Mosher et al. 1992, Knösche 1997), both of which have been often used in other single source sensitivity investigations (Hallez et al. 2008, Dannhauer et al. 2010). Therefore, we cannot exactly determine which part of the placement and angular errors was due to PEM and CEM differences and which part to the limitations of the used inverse procedure. However, the PEM versus CEM forward modeling results of this study and also our present experience with the implemented inverse reconstruction procedure, suggests that the larger part of the presented errors should be due to the differences between PEM and CEM.

The significance of the placement and angular errors obtained vary a lot with regard to the practical viewpoint of source localization. With the smallest applied electrode diameter (6 mm), PE_k and AE_k were clearly negligibly small. Their largest documented maximum values were 1.90 mm PE_k and 1.83° AE_k, and their respective mean values were smaller than $1.62 \cdot 10^{-4}$ mm PE_k and $1.57 \cdot 10^{-4}$ ° AE_k. With an electrode diameter of 12 mm, the maximum values were several times larger: 15.3 mm PE_k and 31.1° AE_k. Even more substantial errors, 25.8 mm PE_k and 54.8° AE_k, were recorded for the electrode diameter of 18 mm. A placement error of several tens of millimeters, which occurred with the 12 mm and 18 mm diameters, is a crucial error in many clinical applications as the sources can be localized in the wrong brain areas. It seems reasonable to us, that since a maximum and mean RDM_k of about 0.11 and 0.05, respectively (see table 1) can lead to single source localization errors as discussed above, our assumption, that the larger part of the presented placement and angular errors are due to the differences between PEM and CEM, seems to be strengthened. A recent study (Dannhauer et al. 2010) related similar RDM forward modeling errors (see their figure 2) to goal function scan inverse reconstruction errors in the same range (see their figure 5). Hence, using the CEM instead of the PEM in forward simulation might lead to essential differences in inverse estimates, when the electrode diameter is at least 12 mm and the applied ECI is low enough ($Z \leq 1\ \Omega\mathrm{m}^2$). Additionally, the mean values of PE_k and AE_k reveals that the amount of the centimeter-scale placement errors was much higher for the 18 mm electrode than for its 12 mm counterpart. The largest reported mean values were 0.363 mm PE_k and 0.475° AE_k, for the 12 mm electrode, whereas with 18 mm diameter electrode, they were 7.83 mm PE_k and 8.88° AE_k.

The ECIs can be coarsely related to the electrode impedances expressed in Ohms via the concept of ACI defined in Section 2.1. Using a round value of 1 cm^2 as the electrode surface area, the suggested limits of the extremely low and high impedances, i.e. $10^{-2}\ \Omega\mathrm{m}^2$ and $10^{2}\ \Omega\mathrm{m}^2$, correspond to ACIs 100 Ω and 1 MΩ, respectively. Of these, the lower limit (100 Ω) coincides with the guideline value given by the American Clinical Neurophysiology Society (American Clinical Neurophysiology Society 2006*b*) for clinical EEG, whereas the upper limit suggested here is much higher than that given in the corresponding guidelines (10 kΩ and $\leq$ 5 kΩ pre-measurement) in (American Clinical Neurophysiology Society 2006*b*, American Clinical Neurophysiology Society 2006*a*). The guidelines for the maximal impedance have been determined mainly based on the average performance of an EEG amplifier (Niedermeyer & da Silva 2004). However, an earlier study (Ferree et al. 2001) shows that excellent EEG signals can be recorded with electrode impedances many times higher (e.g. 40 kΩ) than the guideline values, if the input-impedance is high enough (e.g. 200 MΩ). With regard to the impedances of around 5 kΩ, frequently found in clinical studies, the most relevant value utilized in this study for the electrode diameters of 12 mm and 18 mm can be estimated to be $Z = 1\ \Omega\mathrm{m}^2$, which corresponds to ACI of 8.8 and 3.9 kΩ, respectively. With the smallest diameter electrode 6 mm, the best correspondence to 5 kΩ was obtained at $Z = 0.1$ $\Omega\mathrm{m}^2$ (3.5 kΩ ACI).

Finally, the skin-electrode contact impedance of dry electrodes, that function without any "wet" gel electrolyte on the electrode contact surfaces, can be many times higher than that of the conventional electrodes, e.g. several tens of kΩ, and the diameter can be rather large, e.g. 16 mm (Fiedler et al. 2011). With regard to dry electrodes, the present results suggest the following two points. Firstly, since the relative norm RN, which indicates the captured signal power, was found to grow along with the impedance, the signal amplitudes measured with high-impedance electrodes can be slightly higher than those measured with conventional ones, as observed in (Fiedler et al. 2011). Secondly, it seems that even with ACIs considerably over 10 kΩ the differences between the CEM and PEM forward simulations can be essential, if the electrode diameter is large. For example, RE and RDM obtained with 18 mm diameter and $Z = 10\ \Omega\text{m}^2$ (ACI 39 kΩ) were slightly larger (0.0643 and 0.0318) than those (0.0464 and 0.0192) obtained with 12 mm diameter and $Z = 1\ \Omega\text{m}^2$ (ACI 8.8 kΩ), respectively. In addition to dry and wet skin contact electrodes there exists various other electrode types as well, such as subdermal needle electrodes and depth electrodes, which are used to record electric potentials beneath the skin and directly from the brain, respectively. Applying the CEM for those may be possible but requires further work.

6. Conclusion and outlook

According to the present numerical results, it is suggested that the ECI can be labeled as extremely low (maximal shunting), intermediate, or extremely high (minimal shunting) based on whether it is below $10^{-2}\ \Omega\text{m}^2$, between $10^{-2}\ \Omega\text{m}^2$ and $10^{2}\ \Omega\text{m}^2$ or above $10^{2}\ \Omega\text{m}^2$, respectively. It is also suggested that, from the viewpoint of the EEG inverse problem, essential differences between the CEM and the PEM can occur with ECI of $\leq 1\ \Omega\text{m}^2$ and ACI of ≤ 5 kΩ together with an electrode diameter ≥ 12 mm. Further, the shunting effects that cause the differences will be close to maximal below an ECI value of $10^{-2}\ \Omega\text{m}^2$ and ACI of 100 Ω. It also seems that the use of high-impedance electrodes can be advantageous for the captured signal power, and that the differences between the CEM and PEM forward simulations can be essential even with ACIs considerably over 10 kΩ, if the electrode diameter is large, e.g. ≥ 18 mm.

Our results raise the prospect of the following future investigations: As the impedances and the electrode surfaces that cause larger differences are realistic, and comparable to those of clinical studies, comparing the CEM and the PEM with clinical study data may provide important direction for the future work. Another future approach may be a deeper study on the association between the ECI and ohmic electrode impedances, especially, concerning different electrode shapes, such as the rings in addition to the disks. Additionally, utilizing the CEM to optimize the contact impedance, for parameters such as the signal-to-noise ratio, can provide an interesting new research target. A current limitation of our inverse effect results is that we could not yet quantify which part of the localization and orientation errors is due to the sophisticated interplay between impedance value, electrode surface and volume conduction, especially the effect of the strongly folded cortical surface in our realistic headmodel, and which part is due to the limitations of our current implementation to the inverse problem. For these reasons, we are planning to implement other inverse approaches and better quantify through a comparison of inverse results of the new implementations and their interplay with the Raviart-Thomas sources and the CEM forward approach in the realistic FE head model.

7. Acknowledgements

This research was supported by the Academy of Finland, project no 136412, and by the German Research Foundation (DFG), projects WO1425/2-1 and WO1425/3-1. The authors would like to thank H. Kugel (Department of Clinical Radiology, University of Münster, Germany) for the measurement of the MRI and A. Janssen, S. Rampersad (both Department of Neurology and Clinical Neurophysiology, Radboud University Nijmegen, the Netherlands) and B. Lanfer (Institute for Biomagnetism and Biosignalanalysis, University of Münster, Germany) for their help in setting up the realistic head model.

Appendix. Weak form of the CEM boundary value problem

The weak form (2) can be obtained by first integrating by parts the equation $\nabla\cdot(\sigma\nabla u) = \nabla\cdot\mathbf{J}^p$ multiplied by $v \in H^1(\Omega)$, and after that, applying the CEM boundary conditions (1) to the resulting boundary integral term. Integration by parts yields the equation $\int_\Omega \sigma\nabla u\cdot\nabla v\, dV - \int_{\partial\Omega} v(\sigma\nabla u)\cdot\mathbf{n}\, dS = -\int_\Omega(\nabla\cdot\mathbf{J}^p)v\, dV$, in which the second integral term on the left-hand side can be written as $\int_{\partial\Omega} v(\sigma\nabla u)\cdot\mathbf{n}\, dS = \sum_{\ell=1}^L \int_{e_\ell} v(\sigma\nabla u)\cdot\mathbf{n}\, dS = \sum_{\ell=1}^L \int_{e_\ell} v(U_\ell - u)/Z_\ell\, dS$ resulting from the first boundary condition in (1) as well as from the third one written in the form $\sigma\nabla u\cdot\mathbf{n} = (U_\ell - u)/Z_\ell$. Now, it follows from $U_\ell = (\int_{e_\ell} u\, dS)/(\int_{e_\ell} dS)$ or equivalently from $\int_{e_\ell}(U_\ell - u)\, dS = 0$, implied by the second and third condition in (1), that further $\sum_{\ell=1}^L \int_{e_\ell} v(U_\ell - u)/Z_\ell\, dS = -\sum_{\ell=1}^L \int_{e_\ell}(u - U_\ell)(v - V_\ell)/Z_\ell\, dS$ for any set of real-valued constants $V_1, V_2, \ldots, V_L$. That is, the weak form

$$\int_\Omega \sigma\nabla u\cdot\nabla v\, dV + \sum_{\ell=1}^{L}\frac{1}{Z_\ell}\int_{e_\ell}(U_\ell - u)(V_\ell - v)\, dS = -\int_\Omega(\nabla\cdot\mathbf{J}^p)v\, dV \quad (A.1)$$

must be satisfied for all $v \in H^1(\Omega)$ and $V_\ell \in \mathbb{R}$, $\ell = 1, 2, \ldots, L$. The left-hand side of (A.1) can be shown to constitute a continuous and coercive bilinear form in $H^1(\Omega) \oplus \mathbb{R}^L$ (Vauhkonen 1997, Somersalo et al. 1992), and hence (A.1) is uniquely solvable for any $\mathbf{J}^p$ with a square integrable divergence according to the Lax-Milgram theorem (Braess 2001). Furthermore, substituting $U_\ell = (\int_{e_\ell} u\, dS)/(\int_{e_\ell} dS)$ into (A.1) yields the form (2), which in turn gives the formulas (4)–(7) via the Ritz-Galerkin method (Braess 2001).

References

Akhtari M, Bryant H, Marmelak A, Flynn E, Heller L, Shih J, Mandelkern M, Matlachov A, Ranken D, Best E, DiMauro M, Lee R & Sutherling W 2002 *Brain Top.* **14**(3), 151–167.

American Clinical Neurophysiology Society 2006*a* *Journal of Clinical Neurophysiology* **23**(2), 86–91.

American Clinical Neurophysiology Society 2006*b* *Journal of Clinical Neurophysiology* **23**(2), 97–104.

Baillet S, Marin G, Garnero L & Hugonin J 1999 *IEEE Trans. Biomed. Eng.* **46**(5), 522–534.

Baumann S, Wozny D, Kelly S & Meno F 1997 *IEEE Trans Biomed. Eng.* **44**(3), 220–223.

Boon P, D'Have M, Vanrumste B, Van Hoey G, Vonck K, Van Walleghem P, Caemart J, Achten E & De Reuck J 2002 *J. Clin. Neurophysiol.* **19**(5), 461–468.

Braess D 2001 *Finite Elements* Cambridge University Press Cambridge.

Bruno P, Vatta F, Minimel S & Inchingolo P 2004 *in* 'Proc. of the 26th Annual Int. Conf. IEEE Engineering in Medicine and Biology Society' San Francisco, USA, Sep. 1-5, http://www.ucsfresno.edu/embs2004.

Bruno P, Vatta F, Mininel S & Inchingolo P 2003 *Biomedical Sciences Instrumentation* **39**, 59–64.

Calvetti D, Hakula H, Pursiainen S & Somersalo E 2009 *SIAM J. Imaging Sci.* **2**(3), 879–909.

Cheney M, Isaacson D & Newell J C 1999 *SIAM Review* **41**, 85–101.

Cheng K S, Isaacson D, Newell J C & Gisser D G 1989 *IEEE Transactions on Biomedical Engineering* **36**(9), 918–924.

Cook M & Koles Z 2006 *in* 'Proc. of the 28th Annual Int. Conf. of the IEEE Engineering in Medicine and Biology Society' pp. 4536–4539.

Dale A M & Sereno M I 1993 *J. Cogn. Neurosci* **5**, 162–176.

Dannhauer M, Lanfer B, Wolters C & Knösche T 2010 *Human Brain Mapping* **32**(9), 1383–1399. DOI: 10.1002/hbm.21114, PMID: 20690140.

Dassios G, Fokas A & Hadjiloizi D 2007 *Inverse Problems* **23**, 2541–2549.

de Munck J & Peters M 1993 *IEEE Trans Biomed. Eng.* **40**(11), 1166–1174.

Evans L C 1998 *Partial differential equations* American Mathematical Society Rhode Island.

Ferree T C, Luu P, Russell G S & Tucker D M 2001 *Clinical Neurophysiology* **112**(3), 536–544.

Fiedler P, Cunha L T, Pedrosa P, Brodkorb S, Fonseca C, Vaz F & Haueisen J 2011 *Meas. Sci. Technol.* **22**, 124007.

Fuchs M, Wagner M, Wischmann H A, Kohler T, Theissen A, Drenckhahn R & Buchner H 1998 *Electroencephalography and Clinical Neurophysiology* **107**, 93–111.

Hallez H, Vanrumste B, Hese P V, D'Asseler Y, Lemahieu I & de Walle R V 2005 *Phys.Med.Biol.* **50**, 3787–3806.

Hallez H, Vanrumste B, Van Hese P, Delputte S & Lemahieu I 2008 *Phys.Med.Biol.* **53**, 1877–1894.

Haueisen J & Knösche T 2001 *Journal of Cognitive Neuroscience* **13**, 786–792.

Heers M, Rampp S, Kaltenhäuser M, Pauli E, Rauch C, Dölken M & Stefan H 2010 *Seizure* **19**, 397–403.

Hämäläinen M, Hari R, Ilmoniemi R J, Knuutila J & Lounasmaa O V 1993 *Reviews of Modern Physics* **65**, 413–498.

Huang M, Song T, Hagler D, Podgorny I, Jousmaki V, L.Cui, K.Gaa, D.L.Harrington, Dale A, R.R.Lee, J.Elman & E.Halgren 2007 *NeuroImage* **37**, 731–748.

Knösche T 1997 Solutions of the neuroelectromagnetic inverse problem PhD thesis University of Twente, The Netherlands.

Kybic J, Clerc M, Abboud T, Faugeras O, Keriven R & Papadopoulo T 2005 *IEEE Trans. Med. Imag.* **24**(1), 12–18.

Lanfer B, Scherg M, Dannhauer M, Knösche T & Wolters C 2010 *in* 'Proc. of the 16th Annual Meeting of the Organization for Human Brain Mapping' Barcelona, Spain, June 6-10. http://www.humanbrainmapping.org/barcelona2010/.

Lew S, Wolters C, Dierkes T, Röer C & MacLeod R 2009 *Applied Numerical Mathematics* **59**(8), 1970–1988. http://dx.doi.org/10.1016/j.apnum.2009.02.006, NIHMSID 120338, PMCID: PMC2791331.

Meijs J, Weier O, Peters M & van Oosterom A 1989 *IEEE Trans Biomed. Eng.* **36**, 1038–1049.

Monk P 2003 *Finite Element Methods for Maxwell's Equations* Clarendon Press Oxford, UK.

Mosher J, Lewis P & Leahy R 1992 *IEEE Trans Biomed. Eng.* **39**(6), 541–557.

Niedermeyer E & da Silva F 2004 *Electroencephalography: Basic Principles, Clinical Applications, and Related Fields* Lippincot Williams & Wilkins.

Ollikainen J, Vauhkonen M, Karjalainen P A & Kaipio J P 2000 *Medical Engineering & Physics* **22**, 535–545.

Oostenveld R & Oostendorp T 2002 *Hum Brain Map.* **17**(3), 179–192.

Phillips C, Rugg M D & Friston K J 2002 *NeuroImage* **17**, 287–301.

Pursiainen S 2008*a* *Computational methods in electromagnetic biomedical inverse problems* Vol. Espoo *Dissertation* Helsinki University of Technology.

Pursiainen S 2008*b* *Journal of Physics: Conference Series* **124**(1), 012041 (11pp).

Pursiainen S, Sorrentino A, Campi C & Piana M 2011 *Inverse Problems* **27**(4), 045003 (18pp).

Ramon C, Schimpf P & Haueisen J 2006 *BioMedical Engineering OnLine* **5**(10). doi:10.1186/1475-925X-5-10.

Ramon C, Schimpf P, Haueisen J, Holmes M & Ishimaru A 2004 *Brain Topography* **16**(4), 245–248.

Sadleir R & Argibay A 2007 *Ann.Biomed.Eng.* **35**(10), 1699–1712.

Sarvas J 1987 *Physics in Medicine and Biology* **32**(1), 11.

Scherg M & von Cramon D 1985 *Electroenc. Clin. Neurophysiol.* **62**, 32–44.

Schimpf P, Ramon C & Haueisen J 2002 *IEEE Trans Biomed. Eng.* **49**(5), 409–418.

Sharon D, Hämäläinen M S, Tootell R, Halgren E & Belliveau J W 2007 *NeuroImage* **36**(4), 1225–1235.

Solin P, Segeth K & Dolezel I 2003 *Higher-Order Finite Element Methods* Chapman & Hall / CRC Boca Raton.

Somersalo E, Cheney M & Isaacson D 1992 *SIAM J. Appl. Math.* **52**, 1023–1040.

Stefan H, Hummel C, Scheler G, Genow A, Druschky K, Tilz C, Kaltenhauser M, Hopfengartner R, Buchfelder M & Romstock J 2003 *Brain* **126**(Pt 11), 2396–2405.

Tanzer O, Järvenpää S, Nenonen J & Somersalo E 2005 *Physics in Medicine and Biology* **50**, 3023–3039.

Taubin G 1995 *in* 'Proceedings of the 22nd annual conference on Computer graphics and interactive techniques' ACM pp. 351–358.

The SCIRun Team n.d. SCIRun: A Scientific Computing Problem Solving Environment, Scientific Computing and Imaging Institute (SCI).

Vallaghé S & Papadopoulo T 2010 *SIAM J. Sci. Comput.* **32**(4), 2379–2394.

van den Broek S, Reinders F, Donderwinkel M & Peters M 1998 *Electroenc. Clin. Neurophysiol.* **106**, 522–534.

Vauhkonen M 1997 *Electrical Impedance Tomography and Prior Information* University of Kuopio Kuopio. Dissertation.

Vese L & Chan T 2002 *International Journal of Computer Vision* **50**(3), 271–293.

Wendel K, Narra N, Hannula M, Kauppinen P & Malmivuo J 2008 *IEEE Trans. Biomed. Eng.* **55**(4), 1454–1456.

Wipf D & Nagarajan S 2009 *NeuroImage* **44**, 947–966.

Wolters C, Anwander A, Weinstein D, Koch M, Tricoche X & MacLeod R 2006 *NeuroImage* **30**(3), 813–826. http://dx.doi.org/10.1016/j.neuroimage.2005.10.014, PMID: 16364662.

Wolters C & de Munck J 2007 *Encyclopedia of Computational Neuroscience, Scholarpedia.* **40**(2), 1738. invited review, http://www.scholarpedia.org/article/Volume_Conduction.

Wolters C, Grasedyck L & Hackbusch W 2004 *Inverse Problems* **20**(4), 1099–1116. http://dx.doi.org/10.1088/0266-5611/20/4/007.

Wolters C, Köstler H, Möller C, Härtlein J, Grasedyck L & Hackbusch W 2007 *SIAM J. on Scientific Computing* **30**(1), 24–45. http://dx.doi.org/10.1137/060659053.

Wolters C, Lew S, MacLeod R & Hämäläinen M 2010 *in* 'Proc. of the 44th Annual Meeting, DGBMT' Rostock-Warnemünde, Germany, Oct.5-8, 2010. http://conference.vde.com/bmt-2010.